

Accepted Manuscript

doi: 10.1016/j.epsl.2016.02.047



Frequency modulation reveals the phasing of orbital eccentricity during Cretaceous Oceanic Anoxic Event II and the Eocene hyperthermals

Jiří Laurin^{1*}, Stephen R Meyers², Simone Galeotti³, Luca Lanci³

¹) Institute of Geophysics, Academy of Sciences of the Czech Republic, Boční II/1401, Praha 4, Czech Republic

²) University of Wisconsin – Madison, Department of Geoscience, 1215 W. Dayton St., Madison, WI 53706, USA

³) Dipartimento GeoTeCA, Università degli Studi di Urbino ‘Carlo Bo’, Località Crocicchia, 61029 Urbino, Italy

*) corresponding author; e-mail: laurin@ig.cas.cz

Keywords: orbital eccentricity, cyclostratigraphy, Cenomanian, black shale, Eocene, hyperthermal

HIGHLIGHTS

- Stratigraphic record of eccentricity-related frequency modulation (FM) is examined
- Criteria for distinguishing pristine FM from depositional artifacts are proposed
- FM is employed to interpret the phase of 405-kyr eccentricity in paleo-records
- Eocene hyperthermals occur within ± 90 degrees of 405-kyr eccentricity maxima
- Reduced amplitude of eccentricity and seasonality accompany OAE II

1 **ABSTRACT**

2 Major advances in our understanding of paleoclimate change derive from a precise
3 reconstruction of the periods, amplitudes and phases of the ‘Milankovitch cycles’ of
4 precession, obliquity and eccentricity. While numerous quantitative approaches
5 exist for the identification of these astronomical cycles in stratigraphic data,
6 limitations in radioisotopic dating, and instability of the theoretical astronomical
7 solutions beyond ~50 Myr ago, can challenge identification of the phase
8 relationships needed to constrain climate response and anchor floating
9 astrochronologies. Here we demonstrate that interference patterns accompanying
10 frequency modulation (FM) of short eccentricity provide a robust basis for
11 identifying the phase of long eccentricity forcing in stratigraphic data. One- and two-
12 dimensional models of sedimentary distortion of the astronomical signal are used to
13 evaluate the veracity of the FM method, and indicate that pristine eccentricity FM
14 can be readily distinguished in paleo-records. Apart from paleoclimatic implications,
15 the FM approach provides a quantitative technique for testing and calibrating
16 theoretical astronomical solutions, and for refining chronologies for the deep past.

17 We present two case studies that use the FM approach to evaluate major
18 carbon-cycle perturbations of the Eocene and Late Cretaceous. Interference patterns
19 in the short-eccentricity band reveal that Eocene hyperthermals ETM2 (‘Elmo’), H2,
20 I1 and ETM3 (X; ~52–54 Myr ago) were associated with maxima in the 405-kyr
21 cycle of orbital eccentricity. The same eccentricity configuration favored regional
22 anoxic episodes in the Mediterranean during the Middle and Late Cenomanian
23 (~94.5–97 Myr ago). The initial phase of the global Oceanic Anoxic Event II (OAE II;
24 ~93.9–94.5 Myr ago) coincides with maximum and falling 405-kyr eccentricity, and
25 the recovery phase occurs during minimum and rising 405-kyr eccentricity. On a
26 Myr scale, the event overlaps with a node in eccentricity amplitudes. Both studies
27 underscore the importance of seasonality in pacing major climatic perturbations
28 during greenhouse times.

1. INTRODUCTION

Earth's astronomical parameters control the seasonal and latitudinal distribution of solar radiation entering the Earth's atmosphere, following the periodicities of axial precession (c. 20 kyr), axial obliquity (c. 40 kyr) and orbital eccentricity (95-124 and 405 kyr; e.g., [Berger et al. 1993](#); [Laskar et al. 1993](#)). Attempts to reconstruct the underlying mechanisms of climate forcing – such as glacial/interglacial cyclicity or monsoonal variations – have relied strongly on detailed quantification of the phase of these astronomical parameters as they relate to observed climate events (e.g., [Hays et al. 1976](#); [Ruddiman 2006](#)). Ultimately, the phases of the precessional and obliquity cycles, and their longer modulating terms (e.g., eccentricity), influence the amplitude of seasonality variations (e.g., [Berger et al. 1993](#); [Laskar et al. 1993](#)). The possibility of correlating the onsets and terminations of climate events to the intensity of seasonality is often a key step towards understanding the causal mechanisms of paleoclimate change (e.g., [Imbrie et al. 1993](#); [Lourens et al. 2005](#); [Lunt et al. 2011](#)).

The importance of reconstructing the amplitudes and phases of astronomical parameters from the geologic record has increased following the discovery of very-long term (Myr- and multi-Myr-scale) astronomical influences on past climate (e.g., [Herbert 1997](#); [Pälike et al. 2006](#); [Valero et al. 2014](#); [Wendler et al. 2014](#); [Laurin et al. 2015](#)), which are attributed to the amplitude modulation (AM) of Milankovitch terms. While the existence of these short- and long-term cycles is well established, the phasing is often uncertain (e.g., discussions in [Laurin et al. 2014, 2015](#)), resulting in ambiguity about the specific climate forcing mechanisms involved. The present study introduces a new approach for determining the phase of astronomical forcing preserved in strata, based on interference patterns (constructive and destructive interference of cycles) associated with frequency modulation (FM). Following validation of the approach with a series of one- and two-dimensional stratigraphic models, the technique is applied to evaluate major perturbations to the global carbon cycle associated with Cretaceous Oceanic Anoxic Event II ([Schlanger and Jenkyns, 1976](#)) and the Eocene hyperthermals (e.g., [Lourens et al., 2005](#); [Galeotti et al. 2010](#); [Zachos et al. 2010](#)). In both case studies, the results

unambiguously identify the phasing of 405-kyr eccentricity forcing (and thus the amplitude of seasonality variation), and provide important constraints for anchoring the floating time scales to the theoretical astronomical solutions.

2. BACKGROUND

2.1. Common approaches for determining the phase of astronomical forcing

A number of techniques are commonly used to identify the phase of astronomical forcing from paleoclimate data. These include attempts to directly correlate observed sedimentary rhythms with the theoretical astronomical solutions (Laskar et al. 2004, 2011a,b), often times involving quantitative analysis of AM of lithological or geochemical parameters attributed to astronomical signals (e.g., Lourens et al. 2005; Herbert et al. 1999; Mitchell et al. 2008; Galeotti et al. 2010). However, interpretation of phase by direct comparison of stratigraphic data to the theoretical solutions is often challenged by radioisotopic constraints, which generally exceed the temporal wavelength of the astronomical parameters. In addition to this factor, the chaotic behavior of the Solar System yields instabilities in the theoretical solutions beyond ~50 Myr ago, making it difficult to constrain the phase of insolation beyond the Eocene (Laskar et al. 2011a,b; Westerhold et al. 2012; notable exception to this is the 405-kyr eccentricity cycle, which is predicted to be remarkably stable throughout the Phanerozoic; Laskar et al. 2004, 2011a,b). These challenges notwithstanding, assessment of precession AM and short eccentricity AM in paleoclimate data provides the potential to constrain the phase relationship between climate forcing and response at the eccentricity scale (e.g., Hilgen 1991; Lourens et al. 2005).

Modulations of precessional index and short eccentricity are inherently tied to the phase of short eccentricity and long eccentricity, respectively (Fig. 1). Thus, a theoretically well-founded basis for astronomical phase evaluation exists, through assessment of the recurrence and intensity of distinct lithologies (e.g., Herbert et al. 1999; Lourens et al. 2005; Batenburg et al. 2016), bandpass filtering of inferred astronomical signals (e.g., Lourens et al. 2005; Mitchell et al. 2008; Wu et al. 2013), and complex demodulation (e.g., Shackleton et al. 1995). A difficulty, however, arises

93 when applying the theoretical template (Fig. 1) to real stratigraphic records, which
 94 respond to a multitude of depositional, diagenetic and climatic influences (Meyers et
 95 al. 2008). Stochastic or systematic noise introduced into the sedimentary record
 96 can fabricate an artificial AM in a bandpassed signal (Fig. 2; Huybers and Aharonson
 97 2010), and with an increase in the noise to signal ratio AM of the bandpassed signal
 98 becomes increasingly sensitive to the selection of filter window and bandwidth (Fig.
 99 2b). In point of fact, new astrochronologic testing approaches have been introduced
 100 that specifically address and resolve the problem of artificially generated AM
 101 (Zeeden et al. 2015; Meyers 2015). However, given common practice filtering
 102 approaches in cyclostratigraphy (e.g., relatively narrow bandpass filters; see Zeeden
 103 et al. 2015) and plausible noise and distortions – such as astronomical-scale
 104 fluctuations in sedimentation rate and diagenesis – phase assessment can be severely
 105 compromised (e.g., Figs. 3, 4 and S1.1; see Section 4.1 for more examples). AM can
 106 also be affected by the sampling strategy (Fig. S1.2), non-linearities inherent to the
 107 sedimentary response to climate change (e.g., Laurin et al. 2005), variations in
 108 depositional and/or climatic thresholds and amplitude leakage induced by, for
 109 example, bioturbation (Ripepe and Fischer 1991) or inertia of the system (e.g., the
 110 effect of residence time of carbon in the ocean-atmosphere system). The attribution
 111 of AM to the original astronomical forcing therefore requires tools that would help
 112 to distinguish pristine modulation patterns from artifacts (see also Zeeden et al.
 113 2015 and Meyers 2015). Below we demonstrate that such a tool can be found in the
 114 interference patterns accompanying FM of astronomical signals, which are revealed
 115 by ‘evolutive’ or ‘sliding-window’ spectral techniques.

116

117 **2.2. An alternative approach for determining the phase of astronomical** 118 **forcing: Frequency modulation of the eccentricity signal**

119 Earlier studies (Herbert 1992; Hinnov and Park 1998; Hinnov 2000 and references
 120 therein) have recognized that FM and its phase relationship to AM can provide
 121 critical information about astronomically forced variability in depositional
 122 conditions. Furthermore, changes in spatial (depth-domain) frequency modulation
 123 are now being routinely used to identify sedimentation-rate changes (e.g., Meyers et

124 [al. 2001](#)) and hiatuses ([Meyers and Sageman 2004](#)) in strata. However, little
125 attention has been paid to the application of FM to identify the phase of
126 astronomical forcing (although see [Rial 1999](#)). We focus on the modulation of
127 orbital eccentricity, which forms a relatively long-term astronomical control and as
128 such can be readily examined even in slowly accumulating pelagic and hemipelagic
129 strata. The approach developed here, however, is also applicable to shorter term
130 precession cycles, with stronger requirements on the sampling resolution.

131 The principal changes in the eccentricity of Earth's orbit are related to
132 gravitational perturbations from Venus (g_2), Mars (g_4), and Jupiter (g_5), and occur
133 with periods of 405 kyr (g_2 - g_5), 124 kyr (g_4 - g_2), and 95 kyr (g_4 - g_5 ; where g_2 , g_4 and g_5
134 are fundamental frequencies of the secular system; [Laskar et al. 2004](#); see also
135 [Hinno 2000](#)). These three principal terms are respectively labeled E1, E2 and E3 in
136 this paper. The E2 and E3 variations are themselves composed of a series of closely
137 spaced harmonic components, the most prominent of which have periods of 133.8,
138 131.3, 127.2, 124.6, 100.4, 99.3, 96.6 and 95.2 kyr (solution La2011, interval 80-100
139 Myr ago). Frequency spectra of real stratigraphic records are, however, averaged
140 across a broader frequency band, so the short-eccentricity terms identified in
141 stratigraphic data should be close to 124 kyr and 95 kyr. The ratio of E1 vs. E2 and
142 E3 periods is considered stable within $\pm 5\%$ throughout the Phanerozoic (3.19 ± 0.17
143 and 4.19 ± 0.17 , respectively; [Waltham 2015](#)).

144 As illustrated in [Figure 1](#), the E1 term appears both as a distinct cycle in the
145 frequency domain and as a frequency modulation of the E2 and E3 cycles in the
146 theoretical solution. The E1 eccentricity maxima are accompanied by a constructive
147 interference of E2 and E3, which give rise to a high-amplitude response in the bulk
148 eccentricity signal ([Fig. 1a](#)) with a single frequency maximum approximately
149 halfway between the frequencies of E2 and E3 (~ 9 cycle/Myr, arrows in [Fig. 1e](#)). In
150 contrast, eccentricity minima of the E1 signal are linked to a destructive
151 interference of the E2 and E3 terms, which produce a muted ~ 100 -kyr variance in
152 the bulk eccentricity signal, and are expressed as a distinct split into the E2 and E3
153 signals in the frequency domain ([Fig. 1](#)). Hence, given an adequately preserved
154 eccentricity signal, maxima and minima in E1 eccentricity can be traced by a

155 systematic FM and associated interference patterns in the E2-E3 band ([Fig. 1e](#));
156 these patterns can serve as a tool for the recognition of E1 phasing in paleo-records.

157 The ratio of interfering (E2+E3) and modulating (E1) signals is defined by
158 the theoretical orbital solutions (e.g., La2011; [Laskar et al. 2011b](#)), thus the above
159 relationships can be summarized with the following equation (using the example of
160 E1 modulation of E2+E3):

161

162
$$p_{\text{int}} = p_{\text{E1}} = [(p_{\text{E2}} + p_{\text{E3}})/2] * R \quad (\text{equation 1})$$

163

164 where p_{int} is the spatial period, or recurrence interval of the interference features,
165 p_{E1} is the spatial period of the E1 signal, p_{E2} and p_{E3} are spatial periods of the E2 and
166 E3 signals, respectively, and R is the ratio of the E1 period vs. mean E2-E3 period in
167 the orbital solution La2011 ($R = 3.7 \pm 0.2$ for the Phanerozoic; cf. [Waltham et al.](#)
168 [2015](#)). In the frequency domain, the equation 1 becomes

169

170
$$f_{\text{int}} = f_{\text{E1}} = [(f_{\text{E2}} + f_{\text{E3}})/2]/R \quad (\text{equation 2})$$

171

172 where f_{int} is the spatial frequency of the interference features, f_{E1} is the spatial
173 frequency of the E1 signal, and f_{E2} and f_{E3} are spatial frequencies of the E2 and E3
174 signals, respectively (see [Fig. 1](#)).

175 Before applying this tool to real stratigraphic series, however, it is necessary
176 to evaluate the sensitivity of FM to distortions arising from the climate and
177 depositional system transfer functions ([Meyers et al. 2008](#)). Most importantly, it is
178 essential to show that processes accompanying orbital signal transfer to the
179 sedimentary record cannot fabricate false patterns that could be misinterpreted as
180 FM of the original forcing. The effects of sedimentation rate changes, differential
181 compaction, diagenetic carbonate redistribution and undersampling are examined
182 in Section 4, with one- and two-dimensional numerical models of orbitally driven
183 sedimentation. These models demonstrate that FM is generally a resilient tool for
184 reconstructing the phase of the 405-kyr eccentricity cycle.

185

3. MATERIAL AND METHODS

3.1. Theoretical astronomical solutions

All stratigraphic models discussed in this paper are based on the astronomical solutions La2010d ([Laskar et al. 2011a](#)) and La2011 ([Laskar et al. 2011b](#)). La2010d is a *full solution* that allows reconstructions of eccentricity, obliquity and precession (see appendix of [Wu et al. 2013](#)). The required numerical constraints for calculation of La2011-equivalent precession and obliquity are currently not available; the latest solution La2011 is therefore used only in models with an imposed eccentricity forcing (no precession). The stratigraphic data sets from the Eocene and Cretaceous are compared with orbital eccentricity from La2011 ([Laskar et al. 2011b](#)), which is currently considered the most stable solution for these intervals ([Westerhold et al. 2012](#)).

3.2. Stratigraphic models of astronomical forcing

To test the preservation potential of FM patterns following depositional and post-depositional processes, we develop 7 suites of simple one-dimensional models and one suite of two-dimensional models (30 individual models in total) that simulate astronomically paced changes in sedimentary (lithological or geochemical) parameters. Our focus is on depositional and post-depositional distortions that follow the same rhythm as precessional and eccentricity variations, because these distortions can fabricate false modulation patterns that are most easily confused for pristine astronomical AM and FM. The simplest examples apply constant sedimentation rates ([Figs. S1.2 and S1.8](#)). The effect of changing sedimentation rates is examined with one-dimensional models in which the net sedimentation rate (averaged over 5-kyr time steps) is linearly ([Figs. 3, S1.1, S1.3 and S1.4](#)) or nonlinearly ([Figs. 4, S1.6, S1.7, S1.9 and S1.10](#)) proportional to the astronomical forcing. Both positive and negative relationships between the astronomical forcing and sedimentation rate are modeled. In one group of models ([Fig. S1.4](#)) the sedimentation rate is allowed to decrease to 0 cm/kyr at certain orbital configurations to simulate the effect of hiatuses. A strongly non-linear forcing of sedimentation rate ([Figs. S1.6 and S1.7](#)) is also considered to mimic a differential

217 compaction of layers deposited during different phases of the astronomical cycle.
218 Carbonate redistribution between mud-dominated and carbonate-dominated
219 lithologies would have a similar effect. Selected models are tested for artifacts
220 introduced by different sampling strategies and undersampling (Figs. S1.2 and S1.5).
221 These models explore both imposed eccentricity signals (Figs. 3, 4, 5, S1.1, and S1.8
222 through S1.11) and eccentricity signals originating from a nonlinear transformation
223 of the precessional cycle (Figs. S1.2 through S1.7). Distortions imparted to
224 nearshore and dilution-driven hemipelagic strata by the transfer of astronomical
225 signal via sea-level change (Laurin et al. 2005) are examined with a two-
226 dimensional numerical model (selected output data are shown in Figures 5 and
227 S1.11).

228 Parameters of the one-dimensional models are described and illustrated in
229 Table S1 and Figures 3, 4, and S1. Two-dimensional stratigraphic models were
230 executed with the modeling software “SedTec2000” (Boylan et al. 2002) and are
231 similar in their setup to the “MILex” model of Laurin et al. (2005; for details see Data
232 Repository Items accompanying this paper) with the following differences: (1)
233 length of the model run is 4 Myr, (2) model time step is 2 kyr, and (3) the sea level
234 curve is calculated from the solution La2010d using the following formula: $SL=e*a +$
235 $e1*b$, where e is eccentricity, $e1$ is the bandpassed 405-kyr eccentricity term
236 (Gaussian filter, 2.5 ± 0.5 cycle/Myr), a and b are multipliers (see Table S2). FM
237 patterns were examined on a simulated depth-domain series of the percentage of
238 fine-grained siliciclastics sampled 100 km from the model basin margin.

239

240

241 **3.3. Floating astrochronology development for paleo-records (Cretaceous and** 242 **Eocene), and time series analysis approaches**

243 Spectral estimates for the stratigraphic data and model results are calculated with
244 the multitaper method (MTM; Thomson 1982) using evolutive harmonic analysis
245 (EHA; Meyers et al. 2001). The statistical significance of the EHA spectral results are
246 quantified using the MTM harmonic F-test (for phase-coherent sinusoids; Thomson
247 1982). To conduct astrochronologic testing and comprehensively evaluate a range

of plausible sedimentation models for the Eocene and Cretaceous data sets, Evolutive Average Spectral Misfit (E-ASM; Meyers and Sageman 2007; Meyers 2014) is implemented. This permits an objective and comprehensive test of published astronomical interpretations for the Cretaceous and Eocene data (Lanci et al. 2010; Galeotti et al. 2010), and simultaneously, evaluation of changes in sedimentation rate throughout the study intervals. Unless otherwise indicated, all analyses use three tapers and a time-bandwidth product of 2. The preferred EHA window size for the analysis of E2-E3 interference is 5x the spatial period of the proposed E2-E3 signal.

Preparation of the Cretaceous IRM (Lanci et al. 2010) and Eocene CaCO₃ (Galeotti et al. 2010) data involve resampling on an evenly-spaced grid by piecewise linear interpolation (10 cm for the IRM data and 3 cm for the CaCO₃ data; these values meet or exceed the median sampling interval). All analyses are conducted using the R package 'Astrochron' (Meyers 2014; R Core Team 2015).

4. RESULTS AND DISCUSSION

4.1. Stratigraphic modeling results: Depositional distortions of frequency modulation

The stratigraphic modeling studies indicate that original interference patterns of eccentricity FM are resistant to simple sedimentary distortions, including 20-100% sedimentation-rate changes that are positively or negatively proportional to the precessional and eccentricity forcing. Unlike AM, the interference patterns appear relatively insensitive to undersampling (Figs. S1.2 and S1.5). As regards destabilization of the primary FM, imposed eccentricity variations in sedimentation rate are generally more efficient than precession-paced changes, since the size of the moving window permits averaging across many precessional cycles. A greater distortion is also observed in model setups that employ a non-linear threshold response of sedimentation rate (or differential compaction) and, in particular, when assuming a threshold response for both sedimentation rate and the sedimentary proxy of astronomical variations (Figs. S1.6 and S1.7).

False interference patterns similar to those of the original signal often form

in parts of the distorted record. Importantly, however, in all instances encountered in the one- and two-dimensional models these artifacts either eradicate the strong correlation with the (bandpassed) E1 rhythm, or occur at 'red-' or 'blue-shifted' frequencies. Their recurrence interval is often much longer than the original pacing (Figs. S1.6 and S1.7), which makes them readily recognizable in paleo-data. Somewhat counter intuitively, distorted E2-E3 signals appear more stable in some intervals, as they lack the frequent bifurcations at E1 minima (Fig. S1.6; see also Fig. 5). Other features of the distorted signals include shifting of the interfering frequencies by 5 - 30 % towards or away from the original E2-E3 frequencies (Figs. 4, 5, and S1.6 through S1.11) and the formation of harmonic noise at multiples or divisors of the E2-E3 frequencies (e.g., Figs. 4, S1.2 and S1.6). As discussed below, when such distortions (lack of bifurcations, 'blue/red shift') are observed in paleo-data, they can be used as diagnostics to identify such records as unsuitable for phase assessment.

293

294 **4.2. Stratigraphic modeling results: FM interference patterns as a tool and** 295 **feedback in phase interpretation**

296 Evaluation of the above stratigraphic models suggests that pristine FM patterns can
297 often survive common sedimentary distortions. Stronger distortions accompanying
298 pronounced differential compaction, non-linear fluctuations in sedimentation rate
299 and/or strongly non-linear responses of sedimentary proxies to astronomical
300 forcing can destroy the original patterns and create false, artificial interference
301 features. These artifacts can, however, be readily identified in paleo-data. Thus,
302 confirmation of a primary origin of the FM can be guided by the following features:
303 (1) the recurrence interval of the interference patterns revealed by time-frequency
304 analysis should be identical (within the limits of spectral resolution) with the E1
305 recurrence interval prescribed in equation 1, (2) the interference should occur in
306 the frequency band of the primary interfering signals (E2 and E3), and therefore
307 lack a 'red-' or 'blue-shifted' distortion in excess of the uncertainty in the parameter
308 R (equations 1 and 2; Figs. 4, 5, and S1.7 through S1.11), and (3) if E1 variance is
309 present in the data series (in addition to its modulation of E2+E3), the recurrence

interval of the interference patterns should be in rhythm with the bandpassed E1 signal. Importantly, these relationships are applicable for the evaluation of “untuned” spatial data, and do not require preservation and detection of the modulating signal (E1 in this case). AM and FM patterns not meeting the above criteria should *a priori* be considered distorted and caution should be exercised when attempting to interpret the specific phase of orbital signals, although these records may still be valuable for developing floating astrochronologies and for the interpretation of depositional system response to orbital forcing (e.g., [Laurin et al. 2005](#)).

Therefore, based on these modeling results we propose that interference patterns can be used as a tool to interpret the phasing of 405-kyr eccentricity and/or as a means to distinguish pristine vs. secondary origin of AM and FM of signals obtained by bandpass filtering and amplitude demodulation. By analogy, FM interference patterns in the precessional band can be used to interpret the phase of short eccentricity (E2+E3). For very long records, Myr-scale modulation patterns (e.g., ~2-Myr eccentricity modulation) are a potential target for this method. Intervals that exhibit well-preserved FM of short eccentricity, but are too short for the analysis of Myr-scale FM, might still be instrumental in the assessment of long-term modulation patterns. For example, astronomical solutions indicate that the amplitude within the short-eccentricity band becomes weak and FM is indistinct during Myr-scale eccentricity nodes ([Fig. S2](#)). Continuous series of well-defined FM patterns are therefore unlikely to represent Myr-scale eccentricity minima, and can be interpreted as highs in the Myr-scale modulation. The opposite relationship (i.e., the use of indistinct FM to infer Myr-scale nodes) should not be routinely applied, because the depositional record is subject to a number of processes distorting FM.

The approach described above should be applicable to any well-preserved astronomical records. Data with a low signal-to-noise ratio will likely produce noisy FM patterns, from which it would be challenging to interpret phase with confidence. In these instances, the FM technique can be instrumental in detecting the degree of distortion and avoiding an incorrect interpretation of bandpassed signals.

4.3. Case studies from the Eocene and Cretaceous

Two exquisitely preserved eccentricity records illustrate how pristine FM patterns can be distinguished in real geological data and used to improve paleoclimate interpretation. We focus on intervals associated with major climatic and oceanographic events of the greenhouse world, whose origins remain debated.

4.3.1 Cenomanian black shales and OAE II

The Late Cenomanian to earliest Turonian OAE II was a ~700-kyr long episode of massive removal of organic carbon from the exogenic reservoir (e.g., [Schlanger and Jenkyns 1976](#); [Arthur et al. 1988](#); [Kuypers et al. 2004](#); [Meyers et al. 2012a](#)) in a world characterized by high concentrations of carbon dioxide (and likely other greenhouse gases) in the atmosphere (e.g., [Berner 2006](#)). The increase in carbon burial due to enhanced marine productivity and anoxia (e.g., [Schlanger and Jenkyns 1976](#); [Arthur et al. 1988](#); [Kuypers et al. 2004](#)) was fueled by nutrient fluxes from submarine volcanism ([Snow et al. 2005](#); [Turgeon and Creaser 2008](#); [Flögel et al. 2011](#); [Du Vivier et al. 2014](#)) superimposed upon favorable ocean circulation patterns (e.g., [Trabucho Alexandre et al. 2010](#); [Flögel et al. 2011](#); [Zheng et al. 2013](#)). Several studies suggest an important role for astronomically paced insolation in controlling the timing and structure of OAE II (e.g., [Kuypers et al. 2004](#); [Mitchell et al., 2008](#); [Lanci et al., 2010](#); [Wendler et al., 2014](#); [Laurin et al. 2015](#)). The culmination of OAE II has been shown to coincide with an increased obliquity variance in the low-latitude Atlantic ([Meyers et al. 2012b](#)), which was a major locus of organic carbon accumulation at that time (see review in [Trabucho Alexandre et al. 2010](#)). The timing of OAE II also fits with the rhythm of the long-term, ~1-Myr modulation of axial obliquity (e.g., [Laurin et al. 2015](#)), while some studies propose an ~2-Myr eccentricity influence ([Mitchell et al. 2008](#); [Lanci et al. 2010](#)).

If organic matter accumulation is focused at low latitudes during OAE II (e.g., [Kuypers et al. 2004](#); [Trabucho Alexandre et al. 2010](#)), precession and eccentricity variations are expected to play an important role via a strong control on the monsoon, and thus sedimentation (e.g., [Beckmann et al. 2005](#)). In this regard,

well preserved eccentricity and precession cycles have been described from Cretaceous strata in the Mediterranean (e.g., [De Boer and Wonders 1984](#); [Herbert and Fischer 1986](#)). The Furlo section located in the Umbria-Marche basin, central Italy, has received particular attention as it makes it possible to extend an exquisite eccentricity record of the Middle to Late Cenomanian to the base of the OAE II. Different studies have, however, proposed different phasings of eccentricity variations at this section, with different implications for both the regional climate forcing of anoxia in the Mediterranean and the orbital control on OAE II in general (cf. [Mitchell et al. 2008](#); [Lanci et al. 2010](#)).

Here we reexamine published Isothermal Remanent Magnetization (IRM) data from [Lanci et al. \(2010\)](#). This data set provides a proxy for bottom water oxygenation of the Tethys ocean: high IRM intensities are interpreted to record detrital magnetite preservation under well-oxygenated conditions, while low IRM values are considered a product of magnetite dissolution under poorly oxygenated or euxinic bottom waters ([Lanci et al. 2010](#)). Samples were taken exclusively from limestone lithologies in order to keep the rock-magnetic record independent from lithological variations (see [Lanci et al. 2010](#)); thus the thin (cm-scale) interbedded cherts and black shales, interpreted as largely precessional in their origin ([Mitchell et al. 2008](#)), were not sampled for IRM. The effect of uneven sampling and systematic avoidance of precession-paced black shales in the IRM dataset was tested with a one-dimensional model ([Fig. S1.5](#)). The results indicate that the E2-E3 interference is resistant to this type of undersampling and provides a reliable basis for the interpretation of 405-kyr phasing.

The IRM data show well defined, statistically significant (>94 to >99% F-test significance level) spectral maxima that correspond to the eccentricity terms E1, E2 and E3, as revealed by ASM analysis ([Figs. 6 and S3](#); this confirms the cycle calibration of [Lanci et al. 2010](#)). The EHA spectrogram exhibits well defined frequency patterns originating from the interference of E2 and E3 terms and meets the criteria for pristine modulation outlined in Section 4.2 ([Fig. 6c](#)). Based on the E2-E3 interference patterns we conclude that the ~4-m minima in IRM ([Fig. 6b](#)) correspond to maxima in the 405-kyr eccentricity cycle (in this respect, our

403 interpretation differs from that in [Lanci et al. 2010](#), who proposed the opposite
404 phasing).

405 The size of the EHA window prevents a direct evaluation of interference
406 patterns at and immediately beneath the Bonarelli Level, which marks OAE II at
407 Furlo. To estimate eccentricity phasing at the onset of the Bonarelli Level we
408 integrate the 405-kyr eccentricity bandpass results from the IRM data ([Fig. 6b](#)) with
409 the floating astrochronology of [Mitchell et al. \(2008\)](#); following this approach the
410 onset of the Bonarelli Level is 390 kyr to 420 kyr younger than the last 405-kyr
411 maximum documented with FM (Ce-3; [Figs. 6b,c and S4.1](#)). The high-resolution data
412 of [Batenburg et al. \(2016\)](#) offer alternative timing options. Their tuning #1 is
413 incompatible with radioisotopic constraints in [Eldrett et al. 2015](#) (see [Figure S4.3](#)),
414 but tuning #2, which places the onset of Bonarelli Level only ~340 kyr after the Ce-3
415 maximum ([Fig. 6b](#)), provides a viable possibility. Thus, the onset of Bonarelli Level
416 either predates the following 405-kyr maximum (Ce-2) by 65 kyr, or coincides with
417 this maximum within ± 15 kyr ([Fig. 6](#)). These estimates further imply that the onset
418 of the osmium-isotope excursion ([Turgeon and Creaser 2008; Du Vivier et al. 2014;](#)
419 [Fig. 6b](#)), lithium-isotope excursion ([von Strandmann et al. 2013](#)) and ‘precursor
420 events’ documented locally ([Eldrett et al. 2015](#)) are either coeval with or predate
421 the 405-kyr maximum. Of prime importance for understanding the internal
422 dynamics of OAE II is the onset and acceleration of the positive carbon-isotope
423 ($\delta^{13}\text{C}$) excursion, which should be linked to the rate of global carbon burial (e.g.,
424 [Arthur et al. 1988](#)). The excursion starts immediately above the base of the Bonarelli
425 Level ([Jenkyns et al. 2007; Gambacorta et al. 2015](#)); its onset is therefore considered
426 contemporaneous with the Ce-2 eccentricity maximum within the -65/+15 kyr
427 uncertainty inferred above.

428 Just above the analyzed interval at Furlo, the OAE II is highly condensed;
429 however the details of the event can be examined at other localities. Here we use the
430 high-resolution $\delta^{13}\text{C}_{\text{carb}}$ record from the Eastbourne section ([Paul et al. 1999](#)) and
431 calibrate these data in the time domain based on published astronomical and
432 radioisotopic time scales for this interval ([Sageman et al. 2006; Meyers et al. 2012a;](#)

433 [Ma et al. 2014; Eldrett et al. 2015; see Fig. S4.2](#)). Floating astrochronologies for the
434 Portland and Angus cores ([Sageman et al. 2006; Ma et al. 2014](#)) are correlated to the
435 Eastbourne section using carbon-isotope stratigraphy and biostratigraphy ([Fig.](#)
436 [S4.2](#)). The Eastbourne $\delta^{13}\text{C}_{\text{carb}}$ curve is then aligned with the Furlo record along the
437 base of the positive carbon-isotope excursion ([Jenkyns et al. 2007; Gambacorta et al.](#)
438 [2015; Fig. 6](#)). This correlation is further supported by osmium-isotope data from
439 Furlo and Portland ([du Vivier et al. 2014](#)).

440 Although the uncertainty in numerical dating of the onset and termination
441 of OAE II are on the order of ± 150 kyr ([Meyers et al. 2012a; Eldrett et al. 2015](#)), the
442 uncertainty of the floating time scale duration is an order of magnitude smaller ([Fig.](#)
443 [6](#)) and thus makes it possible to evaluate the timing of OAE II relative to the 405-kyr
444 eccentricity cycle (whose period is stable within 0.16 %; [Laskar et al. 2011a](#)). The
445 integration of phase-calibrated Furlo IRM data with age-calibrated Eastbourne
446 $\delta^{13}\text{C}_{\text{carb}}$ data suggests that the major buildup phase of OAE II (defined by the highest
447 gradient in rising $\delta^{13}\text{C}$; first buildup in [Paul et al. 1999](#)) was coincident with the
448 maximum through declining phases of the 405-kyr eccentricity cycle Ce-2 (and
449 maximum through declining amplitudes of the total E1+E2+E3 eccentricity; [Fig. 6](#)).
450 Drawdown in pCO_2 due to carbon sequestration (e.g., [Barclay et al. 2010](#)) and
451 transient cooling in the Atlantic and Europe ([Voigt et al. 2006; Forster et al. 2007;](#)
452 [Sinninghe Damsté et al. 2010; Zheng et al. 2013; van Helmond et al. 2014;](#)
453 [Gambacorta et al. 2015](#)) occurred during the phase of declining and low eccentricity
454 amplitudes following the Ce-2 maximum ([Fig. 6](#); note that another cooling phase,
455 interpreted by [Gambacorta et al. 2015](#), possibly overlaps with the following 405-kyr
456 minimum). The plateau phase of OAE II ([Paul et al. 1999](#)) coincides with a 405-kyr
457 eccentricity maximum, which according to the latest orbital solution La2011 ([Laskar](#)
458 [et al. 2011b](#)) represents a minimum in the very long term (~ 2.2 Myr) cycle of short-
459 eccentricity AM (red line in [Figure 6a](#)). The recovery phase documented by the
460 onset of declining $\delta^{13}\text{C}$ values c. 80 kyr after the Cenomanian-Turonian boundary
461 starts within ± 70 kyr of a 405-kyr minimum and continues during a resumed rise in
462 the short-eccentricity amplitudes and runup towards another 405-kyr maximum

463 (Fig. 6).

464 Although the Myr-scale modulation in La2011 involves a degree of
465 uncertainty beyond ~50 Myr ago (Westerhold et al. 2012), the possibility of OAE II
466 being centered at a ~2.2-Myr node in eccentricity amplitudes (Fig. 6a) can be
467 evaluated using the FM preservation at Furlo. A comparison of inherent variability
468 in FM (Fig. S2) with the series of 3 to 4 well-defined cycles of 405-kyr modulation
469 beneath OAE II (Fig. 6c) suggests that the interval 0.3 Myr to 1.7 Myr prior to the
470 onset of OAE II is unlikely to accommodate a Myr-scale node. Thus, if the
471 Cenomanian modulation maintains a 2.2-2.4 Myr rhythm as in most of the Cenozoic,
472 then one of the nodes must overlap with the event.

473 The FM signature at Furlo suggests that approximately two-thirds of the
474 black shales and cherts underlying the Bonarelli Level (Fig. 6b) formed at or near
475 maxima in 405-kyr eccentricity. By analogy, most of the shorter-term bundles (and
476 sometimes individual layers) correspond to maxima in the ~100-kyr (E2+E3)
477 eccentricity (Fig. 6a,b), in agreement with the hypothesis of monsoonal forcing of
478 anoxia prior to OAE II in this area (cf. Mitchell et al. 2008). Importantly, black shales
479 and cherts are absent from 405-kyr minima at this section. Considering the overlap
480 of OAE II with one or two 405-kyr minima, the anoxic conditions of OAE II
481 (represented by the Bonarelli Level at Furlo) stand out as a qualitatively distinct
482 response to external forcing, and cannot be considered a mere intensification of the
483 background (monsoonal) variability.

484 The coincidence of the buildup and recovery of OAE II with opposite phases
485 of the 405-kyr eccentricity cycle and the inferred overlap of OAE II with a ~2.2 Myr
486 eccentricity minimum, do not constitute direct evidence for a causal relationship
487 between OAE II and astronomical forcing. Given the role of eccentricity in the global
488 carbon cycle (e.g., Lourens et al. 2005; Pälike et al., 2006; Zachos et al. 2010; Valero
489 et al. 2014), however, it is reasonable to consider a contribution of eccentricity
490 phasing to the internal dynamics of the event. Low eccentricity implies moderate
491 seasonality lacking both extremely low and extremely high seasonal contrasts at the
492 precessional scale. Because the contribution of precessional index (and thus
493 eccentricity) to insolation series is greatest at low latitudes, the reduced eccentricity

provides suitable grounds for both the enhanced obliquity influence during OAE II (Meyers et al. 2012b; Fig. 6e) and increase in the role of higher latitude processes in ocean circulation and the carbon cycle (e.g., Meyers et al. 2012b; Zheng et al. 2013; Laurin et al. 2015). We hypothesize that the shift of intermediate/deep water source towards higher latitudes and its influence on carbon sequestration during OAE II (Meyers et al. 2012b) could be facilitated by subdued short-eccentricity amplitudes during a Myr-scale eccentricity minimum.

A causal role of eccentricity phasing could help to explain the delayed onset of OAE II relative to the initiation of volcanic activity (Turgeon and Creaser 2008; Du Vivier et al. 2014), and the timing of transient cooling episodes (Voigt et al. 2006; Forster et al. 2007; Sinninghe Damsté et al. 2010; Zheng et al. 2013; van Helmond et al. 2014; Gambacorta et al. 2015). Uncertainties in the timing and phasing of the individual segments of OAE II, however, persist, preventing a detailed evaluation of these potential relationships. It is also stressed that OAE II cannot be fully understood without additional controls such as enhanced volcanic nutrient fluxes (Snow et al. 2005; Turgeon and Creaser 2008), changing weathering rates (von Strandmann et al. 2013), particular ocean-circulation patterns (e.g., Trabucchi Alexandre et al. 2010; Flögel et al. 2011) and favorable configuration of the long-term obliquity cycle (e.g., Meyers et al. 2012b; Wendler et al. 2014; Laurin et al. 2015).

4.3.2. Eocene hyperthermals

The Early Eocene interval is marked by a series of brief climate perturbations characterized by warming of sea-surface temperatures, lysocline shallowing and negative carbon-isotope anomalies (e.g., Zachos et al. 2010). Following the Paleocene-Eocene Thermal Maximum (PETM) the most prominent of these events, or hyperthermals, were the ETM2 ('Elmo') and ETM3 ('X'), accompanied by smaller scale events such as H2 and I1 (e.g., Zachos et al. 2010; Fig. 7). The link of hyperthermals to high eccentricity has been proposed in previous studies based on the elapsed time observed between events, and the AM of preserved short-eccentricity cycles (Lourens et al. 2005; Westerhold et al. 2007; Galeotti et al.

525 [2010](#)). The possibility of low-eccentricity forcing of hyperthermals was pointed out
526 recently ([Smith et al. 2014](#), their Scenario 1). An independent test of the 405-kyr
527 eccentricity phasing of the hyperthermals is conducted here through evaluation of
528 FM.

529 Carbonate-content data from the Contessa section, Umbria-Marche basin
530 ([Galeotti et al. 2010](#)) show statistically significant power-spectral maxima (>98% F-
531 test confidence level) corresponding to the E1, E2 and E3 terms, as calibrated by
532 ASM analysis ([Figures 7c and S5](#); this confirms the cycle calibration of [Galeotti et al.](#)
533 [2010](#)). In the upper half of the section, spatial expression of the E2 and E3 cycles
534 suggests systematic interferences associated with E1. By analogy with the above
535 stratigraphic models ([Section 4.2](#)), the intervals of positive interference are
536 interpreted as maxima in the 405-kyr eccentricity cycle. These patterns suggest that
537 the AM studied by [Galeotti et al. \(2010\)](#) is indeed close to the primary modulation of
538 the eccentricity signal. The hyperthermals ETM2 ('Elmo'), I1 and ETM3 ('X') overlap
539 with broad intervals of positive interference in the E2-E3 band. The event H2 is
540 offset towards a phase of negative interference, but none of these hyperthermals
541 overlaps with a minimum in the 405-kyr eccentricity (E1min in [Figure 7](#)). It can be
542 concluded that all events (except the PETM, which can not be evaluated here) occur
543 within 100 kyr (± 90 degrees) of 405-kyr maxima, which is in agreement with the
544 hypotheses invoking a causal role for pronounced seasonal extremes in the forcing
545 mechanism (cf. [Lourens et al. 2005](#); [Lunt et al. 2011](#); [Galeotti et al. 2010](#); [Zachos et](#)
546 [al. 2010](#)).

547

548

549 **5. CONCLUSIONS**

550 Interference patterns accompanying FM in the short-eccentricity band (~95 and
551 124 kyr) provide a robust basis for distinguishing pristine AM and FM from
552 depositional artifacts, and thus make it possible to interpret the phase of
553 astronomical forcing. Pristine FM is marked by a systematic interference of the ~95-
554 kyr and ~124-kyr terms that occur with a 405-kyr rhythm; even if the stratigraphic
555 record lacks a distinct 405-kyr cycle, the interference patterns should follow the

periodicity $p_{\text{int}} = [(p_{i2} + p_{i3})/2] * (3.7 \pm 0.2)$, where p_{i2} and p_{i3} are the spatial periods, i.e., reciprocals of spatial frequencies, of the interfering components (i.e., ~124 and ~95 kyr eccentricity; cf. [Rial 1999](#)). Distortions in the modulation related to climate/depositional system response and sampling lack this rhythm and/or exhibit a 'red' or 'blue shift' of the interfering frequencies, providing a diagnostic to identify such records as unsuitable for phase assessment. We propose that AM and FM patterns obtained through bandpass filtering and demodulation should be routinely validated using the above criteria, specifically if the phasing of the signal is of interest. This approach is applicable to evaluate any frequency-modulated signal that expresses bifurcations (short eccentricity and precession).

Detection of the 405-kyr eccentricity phasing based on FM helps to constrain the astronomical control on paleoclimate change in intervals lacking a stable astronomical solution and/or high-resolution numerical dating. As an example, the results presented here provide independent support for a high-eccentricity forcing of the Early Eocene hyperthermals ETM2 ('Elmo'), ETM3 ('X'), H2 and I1, suggesting a leading role for pronounced seasonal extremes in destabilizing terrestrial or marine carbon reservoirs (e.g., [Lunt et al. 2011](#); [Zachos et al. 2010](#)) or triggering ventilation of a dissolved organic carbon pool ([Sexton et al. 2011](#)). In contrast to the greenhouse gas emission events associated with Eocene hyperthermals, the same (maximum) eccentricity phase promoted carbon burial in the Mediterranean region during the Middle and Late Cenomanian, prior to the global anoxic event OAE II. A comparison of different regional and global responses to a single orbital configuration superimposed upon a secular transition from the Cretaceous greenhouse towards icehouse should facilitate our understanding of the evolving oceanographic responses to astronomical forcing.

The eccentricity phasing of the late-Cretaceous OAE II is also evaluated. The buildup of the positive carbon-isotope excursion coincides with a maximum and subsequent fall in 405-kyr eccentricity, while the recovery correlates with the opposite (i.e., minimum and rising) phases of the 405-kyr cycle. The body of the event is associated with very weak short eccentricity cycles during a 2.2 Myr eccentricity node, according to the solution La2011 ([Laskar et al. 2011b](#)) and in

agreement with observed FM. This configuration provides a context for the transient cooling, propagation of a high-latitude signal towards the equator and enhanced obliquity variance in this interval, as documented in previous studies (Meyers et al. 2012b). We infer that reduced eccentricity amplitudes and corresponding low seasonality variation played a vital role in the mechanism controlling high productivity, anoxia and efficient carbon sequestration during OAE II.

ACKNOWLEDGEMENTS

This research was supported by the Ministry of Education, Czech Republic (grant LH12041). JL acknowledges support by research program RVO67985530 of the Academy of Sciences of the Czech Republic. SRM acknowledges support from U.S. National Science Foundation award EAR-1151438. J. Laskar kindly provided the La2011 eccentricity solution. We are grateful for the constructive reviews from Sietske Batenburg and an anonymous reviewer, which improved the manuscript.

REFERENCES

- Arthur MA, Dean WE, Pratt LM (1988) Geochemical and climatic effects of increased marine organic carbon burial at the Cenomanian/Turonian boundary. *Nature* 335: 714-717, doi:10.1038/335714a0.
- Barclay RS, McElwain JC, Sageman BB (2010) Carbon sequestration activated by a volcanic CO₂ pulse during Ocean Anoxic Event 2. *Nat. Geosci.* 3: 205-208, doi:10.1038/ngeo757.
- Batenburg SJ, De Vleeschouwer D, Sprovieri M, Hilgen FJ, Gale AS, Singer BS, Koeberl C, Coccioni R, Claeys P, Montanari A (2016) Orbital control on the timing of oceanic anoxia in the Late Cretaceous. *Clim. Past Discuss.*, doi:10.5194/cp-2015-182.
- Beckmann B, Flögel S, Hofmann P, Schulz M, Wagner T (2005) Orbital forcing of Cretaceous river discharge in tropical Africa and ocean response. *Nature* 437: 241-244, doi:10.1038/nature03976.
- Berger A, Loutre M-F, Tricot C (1993) Insolation and Earth's orbital periods. *J. Geophys. Res.* 98 (D6): 10341-10362, doi:10.1029/93JD00222.
- Berner RA (2006) GEOCARBSULF: a combined model for Phanerozoic atmospheric O₂ and CO₂. *Geochim. Cosmochim. Acta* 70: 5653-5664,

doi:10.1016/j.gca.2005.11.032.

Boylan AL, Waltham DA, Bosence DWJ, Badenas B, Aurell M (2002) Digital rocks: linking forward modelling to carbonate facies. *Basin Research* 14: 401-415, doi:10.1046/j.1365-2117.2002.00180.x.

De Boer PL, Wonders AAH (1984) Astronomically induced rhythmic bedding in Cretaceous pelagic sediments near Moria (Italy). *Milankovitch and Climate, Part 1*, ed Berger A, Imbrie J, Hays J, Kukla G, Saltzman B (D. Reidel Publishing Company, Boston, MA), pp. 177-190.

Du Vivier ADC, Selby D, Sageman BB, Jarvis I, Gröcke DR, Voigt S (2014) Marine $^{187}\text{Os}/^{188}\text{Os}$ isotope stratigraphy reveals the interaction of volcanism and ocean circulation during Oceanic Anoxic Event 2. *Earth Planet. Sci. Lett.* 389: 23-33, doi:10.1016/j.epsl.2013.12.024.

Eldrett JS, Ma C, Bergman SC, Lutz B, Gregory FJ, Dodsworth P, Phipps M, Hardas P, Minisini D, Ozkan A, Ramezani J, Bowring SA, Kamo SL, Ferguson K, Macaulay C, Kelly AE (2015) An astronomically calibrated stratigraphy of the Cenomanian, Turonian and earliest Coniacian from the Cretaceous Western Interior Seaway, USA: Implications for global chronostratigraphy. *Cretaceous Research* 56: 316-344, doi: 10.1016/j.cretres.2015.04.010.

Flögel S, Wallmann K, Poulsen CJ, Zhou J, Oschlies A, Voigt S, Kuhnt W (2011) Simulating the biogeochemical effects of volcanic CO_2 degassing on the oxygen-state of the deep ocean during the Cenomanian/Turonian Anoxic Event (OAE2). *Earth Planet. Sci. Lett.* 305: 371-384, doi:10.1016/j.epsl.2011.03.018.

Forster A, Schouten S, Moriya K, Wilson PA, Sinninghe Damsté JS (2007) Tropical warming and intermittent cooling during the Cenomanian/Turonian oceanic anoxic event 2: sea surface temperature records from the equatorial Atlantic. *Paleoceanography* 22: PA1219, doi:10.1029/2006PA001349.

Galeotti S, Krishnan S, Pagani M, Lanci L, Gaudio A, Zachos JC, Monechi S, Morelli G, Lourens L (2010) Orbital chronology of Early Eocene hyperthermals from the Contessa Road section, central Italy. *Earth Planet. Sci. Lett.* 290: 192-200, doi:10.1016/j.epsl.2009.12.021.

Gambacorta G, Jenkyns HC, Russo F, Tsikos H, Wilson PA, Faucher G, Erba E (2015) Carbon- and oxygen-isotope records of mid-Cretaceous Tethyan pelagic sequences from the Umbria-Marche and Belluno Basins (Italy). *Newsletters on Stratigraphy* 48: 299-323, doi: 10.1127/nos/2015/0066.

Hays JD, Imbrie J, Shackleton NJ (1976) Variations in the Earth's Orbit: Pacemaker of the Ice Ages. *Science* 194: 1121-1132, doi:10.1126/science.194.4270.1121.

Herbert TD, Fischer AG (1986) Milankovitch climatic origin of the mid-Cretaceous black shale rhythms in central Italy. *Nature* 321: 739-743.

Herbert TD (1992) Paleomagnetic calibration of Milankovitch cyclicity in Lower Cretaceous sediments. *Earth Planet. Sci. Lett.* 112: 15-28.

Herbert TD (1997) A long marine history of carbon cycle modulation by orbital-climatic changes. *Proc. Natl. Acad. Sci.* 94: 8362-8369.

Herbert TD, Gee J, DiDonna S (1999) Precessional cycles in Upper Cretaceous pelagic sediments of the South Atlantic: Long-term patterns from high-frequency climate variations. *Evolution of the Cretaceous ocean-climate system*, ed

669 Barrera E, Johnson CC (Geological Society of America Special Paper 332), pp
 670 105–120, doi:10.1130/0-8137-2332-9.105.
 671 Hilgen FJ (1991), Astronomical calibration of Gauss to Matuyama sapropels in the
 672 Mediterranean and implication for the geomagnetic polarity time scale. *Earth*
 673 *Planet. Sci. Lett.* 104: 226–244, doi:10.1016/0012-821X(91)90206-W.
 674 Hinnov LA (2000) New perspectives on orbitally forced stratigraphy. *Annu. Rev.*
 675 *Earth Planet. Sci.* 28: 419–475, doi:10.1146/annurev.earth.28.1.419.
 676 Hinnov LA, Park JJ (1998) Detection of astronomical cycles in the stratigraphic
 677 record by frequency modulation (FM) analysis. *J. Sediment. Res.* 68: 524–539.
 678 Huybers P, Aharonson O (2010) Orbital tuning, eccentricity, and the frequency
 679 modulation of climatic precession. *Paleoceanography* 25: PA4228.
 680 Imbrie J, Berger A, Boyle EA, Clemens SC, Duffy A, Howard WR, Kukla G, Kutzbach J,
 681 Martinson DG, McIntyre A, Mix AC, Molino B, Morley JJ, Peterson LC, Pisias
 682 NG, Prell WL, Raymo ME, Shackleton NJ, Toggweiler JR (1993) On the
 683 structure and origin of major glaciation cycles: 2. The 100,000-year cycle.
 684 *Paleoceanography* 8: 699–735, doi:10.1029/93PA02751.
 685 Jenkyns HC, Matthews A, Tsikos H, Erel Y (2007) Nitrate reduction, sulfate
 686 reduction, and sedimentary iron isotope evolution during the Cenomanian-
 687 Turonian oceanic anoxic event. *Paleoceanography* 22: PA3208,
 688 doi:10.1029/2006PA001355.
 689 Kuypers MMM, Lourens LJ, Rijkstra WIC, Pancost RD, Nijenhuis IA, Sinninghe
 690 Damsté JS (2004) Orbital forcing of organic carbon burial in the proto-North
 691 Atlantic during oceanic anoxic event 2. *Earth Planet. Sci. Lett.* 228: 465–482,
 692 doi:10.1016/j.epsl.2004.09.037.
 693 Lanci L, Muttoni G, Erba E (2010) Astronomical tuning of the Cenomanian Scaglia
 694 Bianca Formation at Furlo, Italy. *Earth Planet. Sci. Lett.* 292: 231–237,
 695 doi:10.1016/j.epsl.2010.01.041.
 696 Laskar J, Robutel P, Joutel F, Gastineau M, Correia ACM, Levrard B (2004) A long-
 697 term numerical solution for the insolation quantities of the Earth. *Astron.*
 698 *Astrophys.* 428: 261–285, doi:10.1051/0004-6361:20041335.
 699 Laskar J, Fienga A, Gastineau M, Manche H (2011a) La2010: A new orbital solution
 700 for the long term motion of the Earth. *Astron. Astrophys.* 532: A89,
 701 doi:10.1051/0004-6361/201116836.
 702 Laskar J, Gastineau M, Delisle J-B, Farrés A, Fienga A (2011b) Strong chaos induced
 703 by close encounters with Ceres and Vesta. *Astronomy and Astrophysics* 532:
 704 L4, doi: 10.1051/0004-6361/201117504.
 705 Laskar J, Joutel F, Boudin F (1993) Orbital, precessional, and insolation quantities
 706 for the Earth from –20 Myr to +10 Myr. *Astron. Astrophys.* 270: 522–533.
 707 Laurin J, Čech S, Uličný D, Štaffen Z, Svobodová M (2014) Astrochronology of the
 708 Late Turonian: implications for the behavior of the carbon cycle at the
 709 demise of peak greenhouse. *Earth Planet. Sci. Lett.* 394: 254–269,
 710 doi:10.1016/j.epsl.2014.03.023.
 711 Laurin J, Meyers SR, Sageman BB, Waltham D (2005) Phase-lagged amplitude
 712 modulation of hemipelagic cycles: A potential tool for recognition and
 713 analysis of sea-level change. *Geology* 33(7): 569–572, doi:10.1130/G21350.1.
 714 Laurin J, Meyers SR, Uličný D, Jarvis I, Sageman BB (2015) Axial obliquity control on

the greenhouse carbon budget through middle- to high-latitude reservoirs. *Paleoceanography* 30(2): 133-149, doi:10.1002/2014PA002736.

Lourens LJ, Sluijs A, Kroon D, Zachos JC, Thomas E, Röhl U, Bowles J, Raffi I (2005) Astronomical pacing of late Palaeocene to early Eocene global warming events. *Nature* 435: 1083–1087, doi:10.1038/nature03814.

Lunt DJ, Ridgwell A, Sluijs A, Zachos J, Hunter S, Haywood A (2011) A model for orbital pacing of methane hydrate destabilization during the Palaeogene. *Nat. Geosci.* 4: 775-778, doi:10.1038/ngeo1266.

Ma C, Meyers SR, Sageman BB, Singer BS, Jicha BR (2014) Testing the astronomical time scale for oceanic anoxic event 2, and its extension into Cenomanian strata of the Western Interior Basin (USA). *Geol. Soc. Am. Bul.* 126: 974-989.

Meyers SR (2014) astrochron: An R Package for Astrochronology (Version 0.3.1). <http://www.geology.wisc.edu/~smeyers>.

Meyers SR (2015) The evaluation of eccentricity-related amplitude modulation and bundling in paleoclimate data: An inverse approach for astrochronologic testing and time scale optimization. *Paleoceanography* 30, doi:10.1002/2015PA002850.

Meyers SR, Sageman BB (2004) Detection, quantification, and significance of hiatuses in pelagic and hemipelagic strata. *Earth Planet. Sci. Lett.* 224: 55-72, doi:10.1016/j.epsl.2004.05.003.

Meyers SR, Sageman BB (2007) Quantification of deep-time orbital forcing by average spectral misfit. *Am. J. Sci.* 307: 773–792, doi:10.2475/05.2007.01.

Meyers SR, Sageman BB, Hinnov LA (2001) Integrated quantitative stratigraphy of the Cenomanian-Turonian Bridge Creek Limestone Member using evolutive harmonic analysis and stratigraphic modeling. *J. Sediment. Res.* 71: 628-644.

Meyers SR, Sageman BB, Pagani M (2008) Resolving Milankovitch: Consideration of signal and noise. *Am. J. Sci.* 308: 770–786, doi:10.2475/06.2008.02.

Meyers SR, Siewert SE, Singer BS, Sageman BB, Condon DJ, Obradovich JD, Jicha BR, Sawyer DA (2012a) Intercalibration of radioisotopic and astrochronologic time scales for the Cenomanian-Turonian boundary interval, Western Interior Basin, USA. *Geology* 40: 7-10, doi:10.1130/G32261.1.

Meyers SR, Sageman BB, Arthur MA (2012b) Obliquity forcing of organic matter accumulation during Oceanic Anoxic Event 2. *Paleoceanography* 27: PA3212, doi:10.1029/2012PA002286.

Mitchell RN, Bice DM, Montanari A, Cleaveland LC, Christianson KT, Coccioni R, Hinnov LA (2008) Oceanic anoxic cycles? Orbital prelude to the Bonarelli Level (OAE 2). *Earth Planet. Sci. Lett.* 26: 1–16, doi:10.1016/j.epsl.2007.11.026.

Pälike H, Norris RD, Herrle JO, Wilson PA, Coxall HK, Lear CH, Shackleton NJ, Tripati AK, Wade BS (2006) The heartbeat of the Oligocene climate system *Science* 314: 1894–1898.

Paul CRC, Lamolda MA, Mitchell SF, Vaziri MR, Gorostidi A, Marshall JD (1999) The Cenomanian–Turonian boundary at Eastbourne (Sussex, UK): a proposed European reference section. *Palaeogeogr. Palaeoclimatol. Palaeoecol.* 150: 83–121, doi:10.1016/S0031-0182(99)00009-7.

R Core Team (2015) R: A language and environment for statistical computing. R

Foundation for Statistical Computing, Vienna, Austria. <http://www.R-project.org/>.

Rial JA (1999) Pacemaking the ice ages by frequency modulation of Earth's orbital eccentricity. *Science* 285: 564-568.

Ripepe M, Fischer AG (1991) Stratigraphic rhythms synthesized from orbital variations. *Sedimentary Modeling: Computer Simulations and Methods for Improved Parameter Definition*, eds Franseen K, Watney WL, Kendall CGStC, Ross W (Kansas State Geol. Surv. Bull. 233), pp. 335-344.

Ruddiman WF (2006) What is the timing of orbital-scale monsoon changes? *Quat. Sci. Rev.* 25: 657-658, doi:10.1016/j.quascirev.2006.02.004.

Sageman BB, Meyers SR, Arthur MA (2006) Orbital time scale and new C-isotope record for Cenomanian-Turonian boundary stratotype. *Geology* 34: 125-125.

Schlanger S, Jenkyns H (1976) Cretaceous oceanic anoxic events: causes and consequences. *Geologie en mijnbouw* 55: 179-184.

Sexton PF, Norris RD, Wilson PA, Pälike H, Westerhold T, Röhl U, Bolton CT, Gibbs S (2011) Eocene global warming events driven by ventilation of oceanic dissolved organic carbon. *Nature* 471: 349-352, doi:10.1038/nature09826.

Shackleton NJ, Hagelberg T.K, Crowhurst SJ (1995) Evaluating the success of astronomical tuning: Pitfalls of using coherence as a criterion for assessing pre-Pleistocene timescales. *Paleoceanography* 10(4): 693-697, doi:10.1029/95PA01454.

Sinninghe Damsté JS, van Bentum EC, Reichart G-J, Pross J, Schouten S (2010) A CO₂ decrease-driven cooling and increased latitudinal temperature gradient during the mid-Cretaceous Oceanic Anoxic Event 2. *Earth Planet. Sci. Lett.* 293: 97-103, doi:10.1016/j.epsl.2010.02.027.

Smith ME, Carroll AR, Scott JJ, Singer BS (2014) Early Eocene carbon isotope excursions and landscape destabilization at eccentricity minima: Green River Formation of Wyoming. *Earth Planet. Sci. Lett.* 403: 393-406, doi:10.1016/j.epsl.2014.06.024.

Snow LJ, Duncan RA, Bralower TJ (2005) Trace element abundances in the Rock Canyon Anticline, Pueblo, Colorado, marine sedimentary section and their relationship to Caribbean plateau construction and oxygen anoxic event 2. *Paleoceanography* 20: PA3005, doi:10.1029/2004PA001093.

Thomson DJ (1982) Spectrum estimation and harmonic analysis. *IEEE Proceedings* 70: 1055-1096, doi:10.1109/PROC.1982.12433.

Trabucho Alexandre J, Tuenter E, Henstra GA, van der Zwan KJ, van de Wal RSW, Dijkstra HA, de Boer PL (2010) The mid-Cretaceous North Atlantic nutrient trap: Black shales and OAEs. *Paleoceanography* 25: PA4201, doi:10.1029/2010PA001925.

Turgeon SC, Creaser RA (2008) Cretaceous oceanic anoxic event 2 triggered by a massive magmatic episode. *Nature* 454: 323-326, doi:10.1038/nature07076.

Valero L, Garcés M, Cabrera L, Costa E, Sáez A (2014) 20 Myr of eccentricity paced lacustrine cycles in the Cenozoic Ebro Basin. *Earth Planet. Sci. Lett.* 408: 183-193, doi:10.1016/j.epsl.2014.10.007.

van Helmond NAGM, Sluijs A, Reichart G-J, Sinninghe Damsté JS, Slomp CP, Brinkhuis H (2014) A perturbed hydrological cycle during Oceanic Anoxic Event 2.

807 *Geology* 42: 123-126, doi:10.1130/G34929.1.

808 Voigt S, Gale AS, Voigt T (2006) Sea-level change, carbon cycling and palaeoclimate
809 during the Late Cenomanian of northwest Europe; an integrated
810 palaeoenvironmental analysis. *Cretaceous Research* 27: 836-858,
811 doi:10.1016/j.cretres.2006.04.005.

812 Waltham D (2015) Milankovitch period uncertainties and their impact on
813 cyclostratigraphy. *J. Sediment. Res.* 85: 990-998, doi:10.2110/jsr.2015.66

814 Wendler JE, Meyers SR, Wendler I, Kuss J (2014) A million-year-scale astronomical
815 control on Late Cretaceous sea-level. *Newsl. Stratigr.* 47: 1-19,
816 doi:10.1127/0078-0421/2014/0038.

817 Westerhold T, Röhl U, Laskar J, Raffi I, Bowles J, Lourens LJ, Zachos JC (2007) On the
818 duration of magnetochrons C24r and C25n and the timing of early Eocene
819 global warming events: implications from the Ocean Drilling Program Leg
820 208 Walvis Ridge depth transect. *Paleoceanography* 22: PA2201.

821 Westerhold T, Röhl U, Laskar J (2012) Time scale controversy: Accurate orbital
822 calibration of the early Paleogene. *Geochem. Geophys. Geosyst.* 13: Q06015,
823 doi:10.1029/2012GC004096.

824 Wu H, Zhang S, Jiang G, Hinnov L, Yang T, Li H, Wan X, Wang C (2013)
825 Astrochronology of the Early Turonian-Early Campanian terrestrial
826 succession in the Songliao Basin, northeastern China and its implications for
827 long-period behavior of the Solar System. *Palaeogeogr., Palaeoclimatol.,*
828 *Palaeoecol.* 385: 55–70.

829 Zachos JC, McCarren H, Murphy B, Röhl U, Westerhold T (2010) Tempo and scale of
830 late Paleocene and early Eocene carbon isotope cycles: Implications for the
831 origin of hyperthermals. *Earth Planet. Sci. Lett.* 299(1–2): 242–249,
832 doi:10.1016/j.epsl.2010.09.004.

833 Zeeden C, Meyers SR, Lourens LJ, Hilgen FJ (2015) Testing astronomically tuned age
834 models. *Paleoceanography* 30: 369-383, doi: 10.1002/2014PA002762.

835 Zheng X-Y, Jenkyns HC, Gale AS, Ward DJ, Henderson GM (2013) Changing ocean
836 circulation and hydrothermal inputs during Ocean Anoxic Event 2
837 (Cenomanian–Turonian): Evidence from Nd-isotopes in the European shelf
838 sea. *Earth Planet. Sci. Lett.* 375: 338-348, doi:10.1016/j.epsl.2013.05.053.

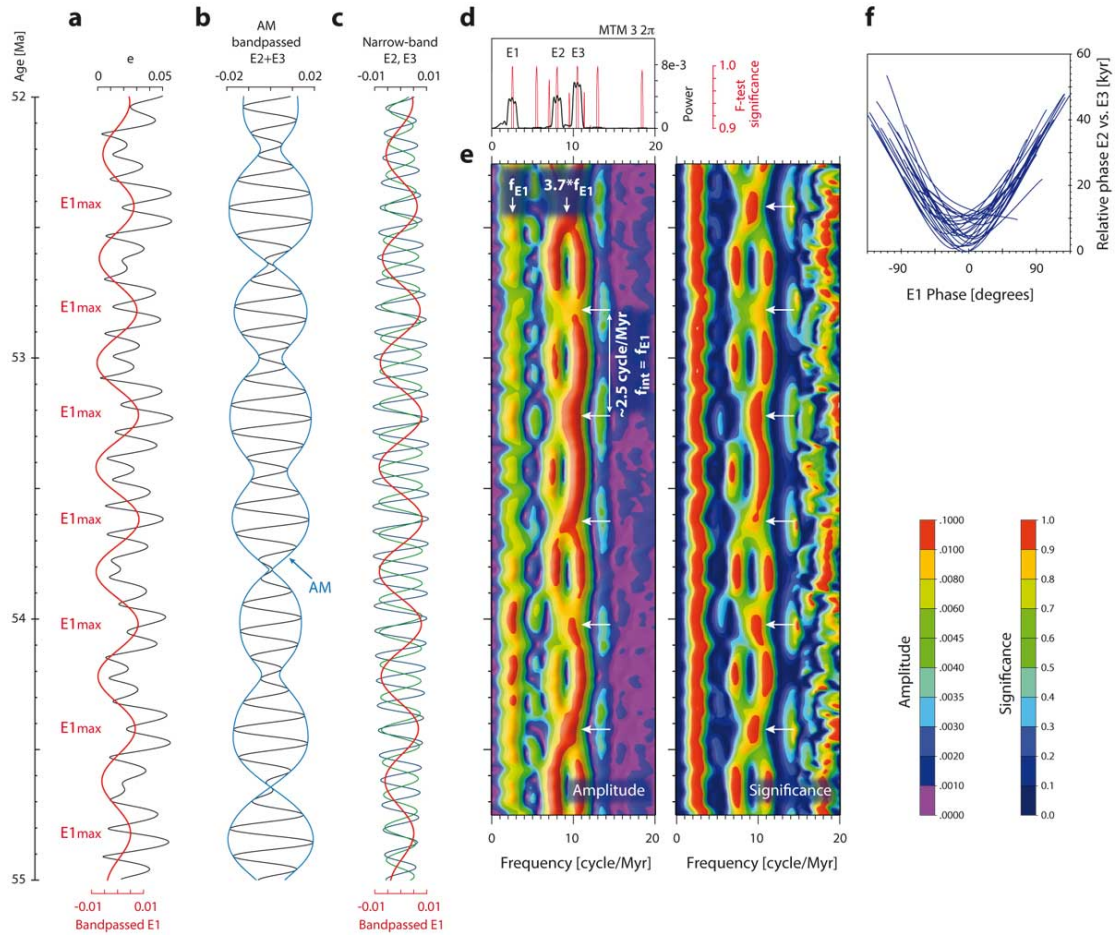


Figure 1. Modulation and phasing of orbital eccentricity. **(a)** Eccentricity (e ; solution La2011, 52-55 Myr ago). Bandpassed 405-kyr term ($E1$; 2.5 ± 0.3 cycle/Myr, Gaussian filter) is shown in red. $E1_{\max}$ = 405-kyr eccentricity maximum. **(b)** Amplitude modulation (AM) of short eccentricity ($E2+E3$; 9.5 ± 3.0 cycle/Myr, Gaussian filter). AM is commonly used as a tool to identify the phase of eccentricity forcing in stratigraphic records. Here we propose that the analysis of AM should be combined with an examination of frequency modulation (FM) and interference patterns that are tightly linked to the phase of the modulating cycle as shown further below: **(c)** Phasing of the main eccentricity components. Narrow-band filtered $E2$ (125 kyr; 8.0 ± 0.3 cycle/Myr, Gaussian filter) in green, and $E3$ (95 kyr; 10.5 ± 0.3 cycle/Myr, Gaussian filter) in black. Note that $E2$ and $E3$ interfere constructively at $E1_{\max}$ (bandpassed $E1$ in red; 2.5 ± 0.3 cycle/Myr, Gaussian filter). **(d)** MTM power spectrum and F-test significance for eccentricity. **(e)** Evolutive Harmonic Analysis (EHA; Meyers et al. 2001) amplitude and F-test significance spectra (MTM 3 2π ; 500-kyr window). White arrows mark intervals of positive interference ('junctions') of $E2$ and $E3$ beats that form at 405-kyr eccentricity maxima. Note that the mean frequency of the interfering components ($E2$ and $E3$) is the 3.7-th multiple of the recurrence frequency of the interference patterns ($f_{\text{int}} \sim 2.5$ cycle/Myr); this ratio serves as a diagnostic feature of pristine eccentricity modulation (see text). **(f)** Scatter plot documenting the relationship between the relative phasing of $E2$ vs. $E3$ (vertical axis) and the phase of 405-kyr cycle. Note that the $E2$ and $E3$ cycles are in phase (i.e., interfere constructively) at 405-kyr maxima (0 deg. phase of $E1$).

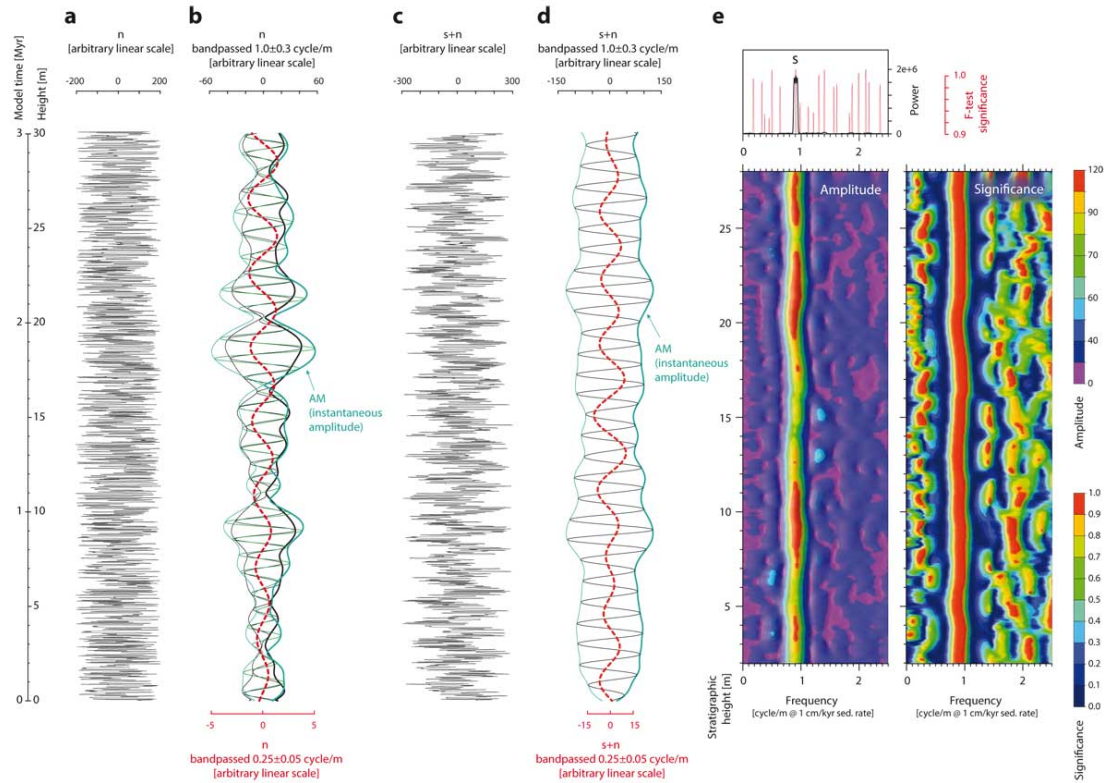


Figure 2. Limitations of the conventional AM approach to phase interpretation. **(a)** Time series consisting of a white noise. Sedimentation rate 1 cm/kyr. Model #1, [Table S1](#). **(b)** White noise filtered in the expected short-eccentricity band. Black lines: Gaussian filter, 1.0 ± 0.3 cycle/m. Green lines: rectangular filter, 1.0 ± 0.3 cycle/m. Dashed red line denotes white noise filtered in the 405-kyr band (Gaussian filter, 0.25 ± 0.05 cycle/m). Note a well-defined AM, which locally resembles the 405-kyr bundling of short-eccentricity cycles. This AM is an artifact of filtering across a ± 0.3 cycle/m bandwidth. **(c)** Time series consisting of a sinusoidal, 110-kyr signal (s) and white noise (n). Model #2, [Table S1](#). **(d)** Time series s+n filtered in the short-eccentricity band (Gaussian filter, 1.0 ± 0.3 cycle/m). Dashed red line: Gaussian filter, 0.25 ± 0.05 cycle/m. The inclusion of noise generates artificial AM that resembles eccentricity bundling in places (e.g., intervals 7-11, or 19-24 m). The conventional AM approach cannot distinguish these types of signal distortion, thus potentially misinterpreting the artificial AM as a signature of 405-kyr modulation (see also [Zeeden et al. 2015](#) and [Meyers 2015](#)). **(e)** Spectral estimates for the series s+n: MTM ($3 \cdot 2\pi$) power spectral and significance estimates for the entire series (top), and EHA (MTM $3 \cdot 2\pi$) amplitude and significance, 4-m moving window. Minor frequency slips are present. However, the artificial AM is not associated with systematic FM and interference patterns that characterize real astronomical signals (compare with [Figure 1](#)).

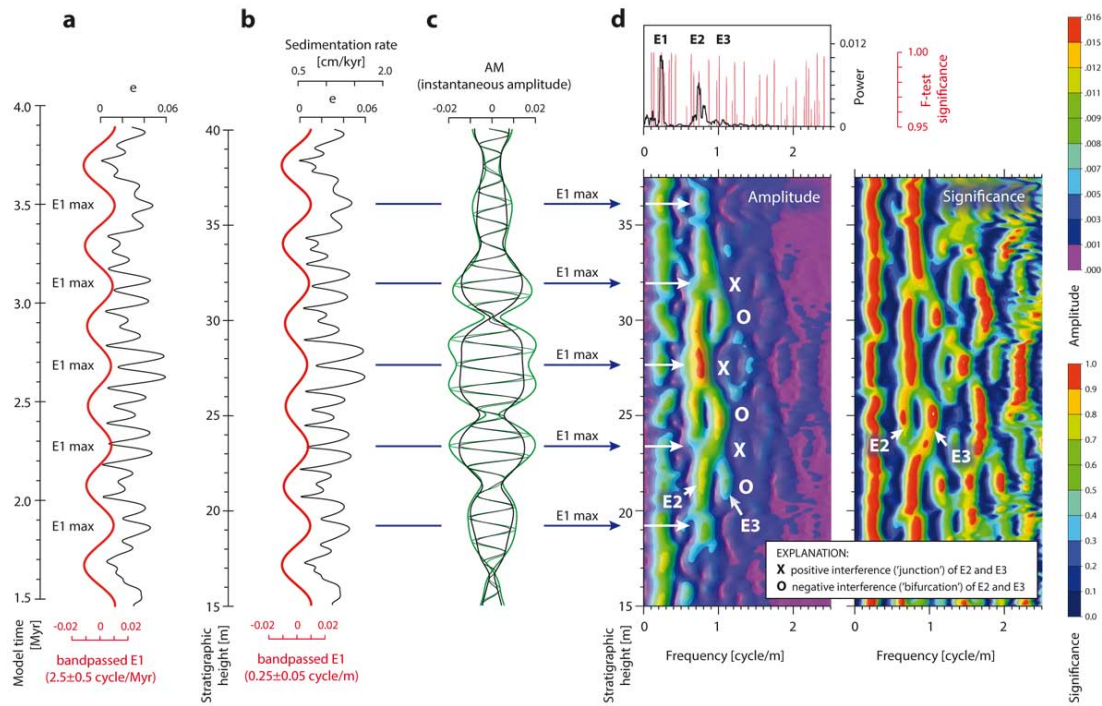
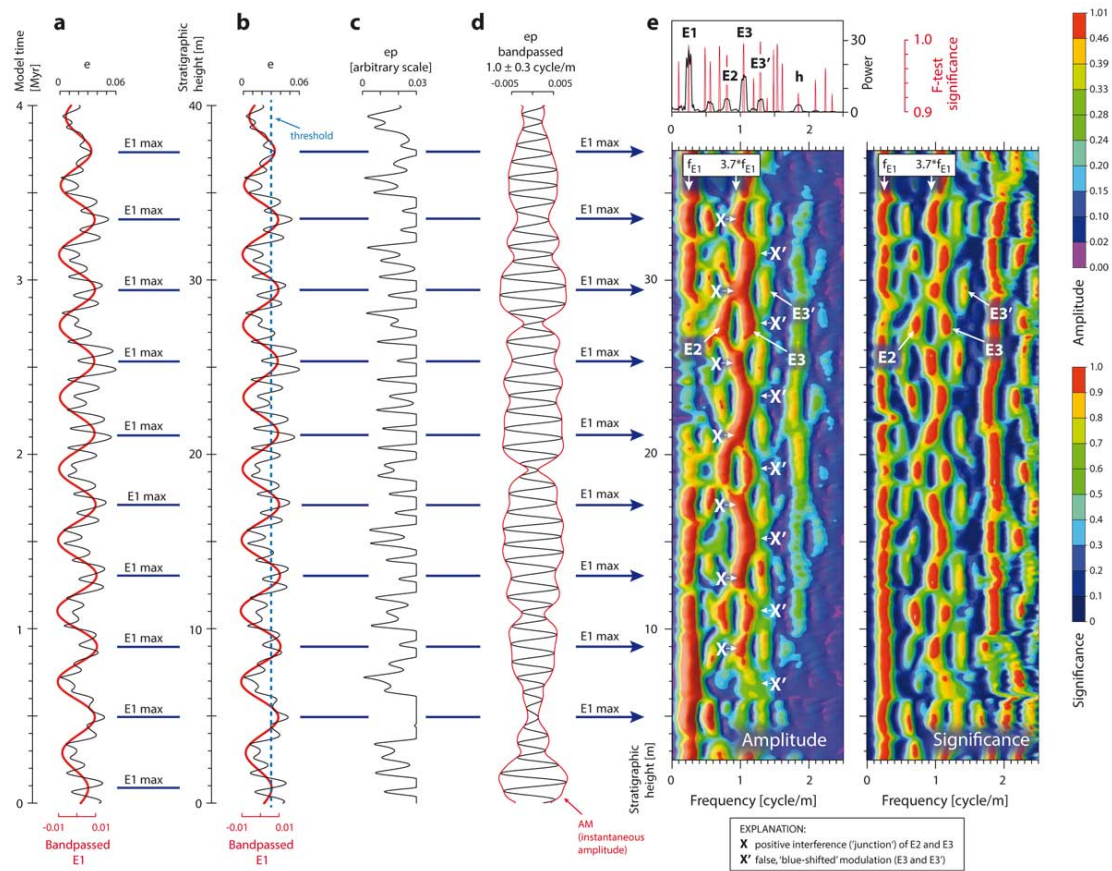
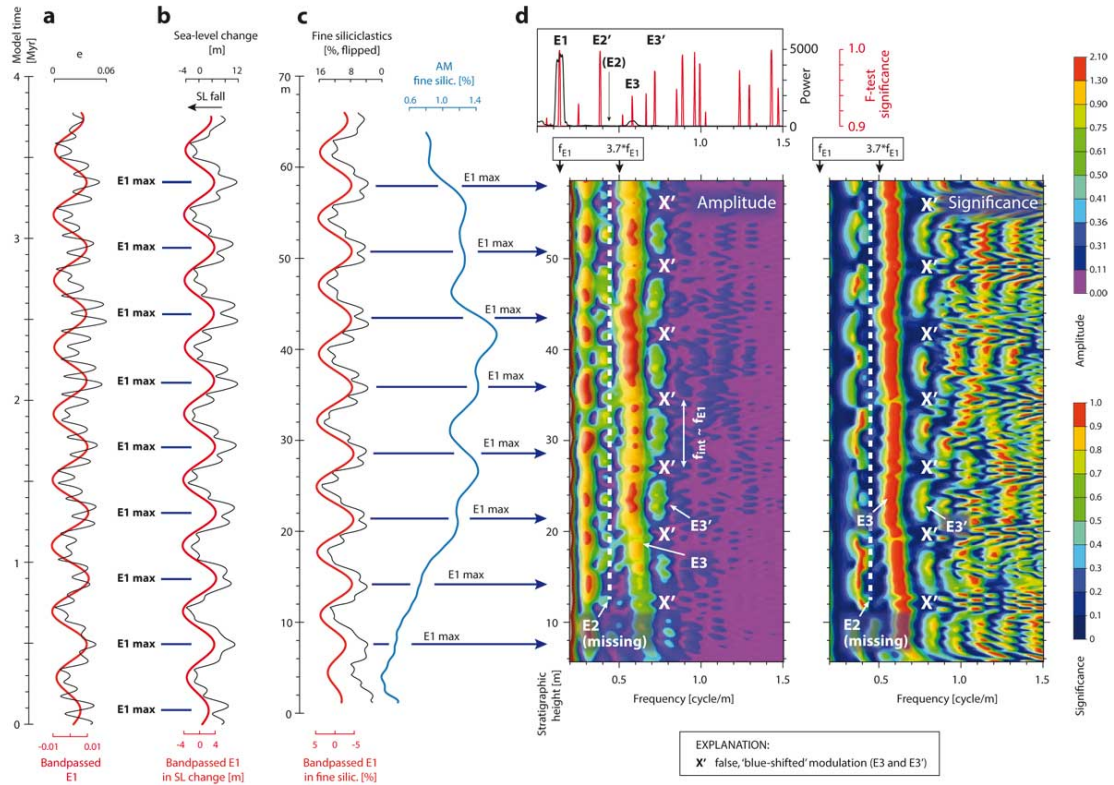


Figure 3. Preservation and distortion of E2-E3 interference. In this model (#4, [Tab. S1](#)), sedimentation rate is linearly proportional to orbital eccentricity. **(a)** Orbital eccentricity (e ; solution La2010d, interval 96-98.5 Ma) plotted against time. Bandpassed 405-kyr eccentricity shown in red (2.5 ± 0.5 cycle/Myr, Gaussian filter). E1 max = 405-kyr maximum. **(b)** Orbital eccentricity and sedimentation rate plotted against stratigraphic height. Bandpassed 405-kyr eccentricity shown in red (0.25 ± 0.05 cycle/m, Gaussian filter). **(c)** AM of the E2+E3 signal in e (0.9 ± 0.3 cycle/m). AM is generally sensitive to the selection of filter parameters (black line: Gaussian filter; green line: rectangular filter), and provides an unstable basis for the interpretation of E1 maxima and minima (see also [Figures 2, 4d, and 5c](#)). The record of FM in time-frequency plots makes it possible to identify distortion: **(d)** Spectral estimates for the parameter e in the depth domain: MTM ($3 \cdot 2\pi$) power spectral and significance estimates for the entire series (top), and EHA (MTM $3 \cdot 2\pi$) amplitude and significance, 5-m moving window. Eccentricity terms E1, E2 and E3 are indicated. Note that 'junctions' (X) and 'bifurcations' (O) originating from the interference of E2 and E3 identify the source of AM and thus facilitate a correct interpretation of the 405-kyr maxima and minima in the orbital forcing. See also [Figure S1.1](#).





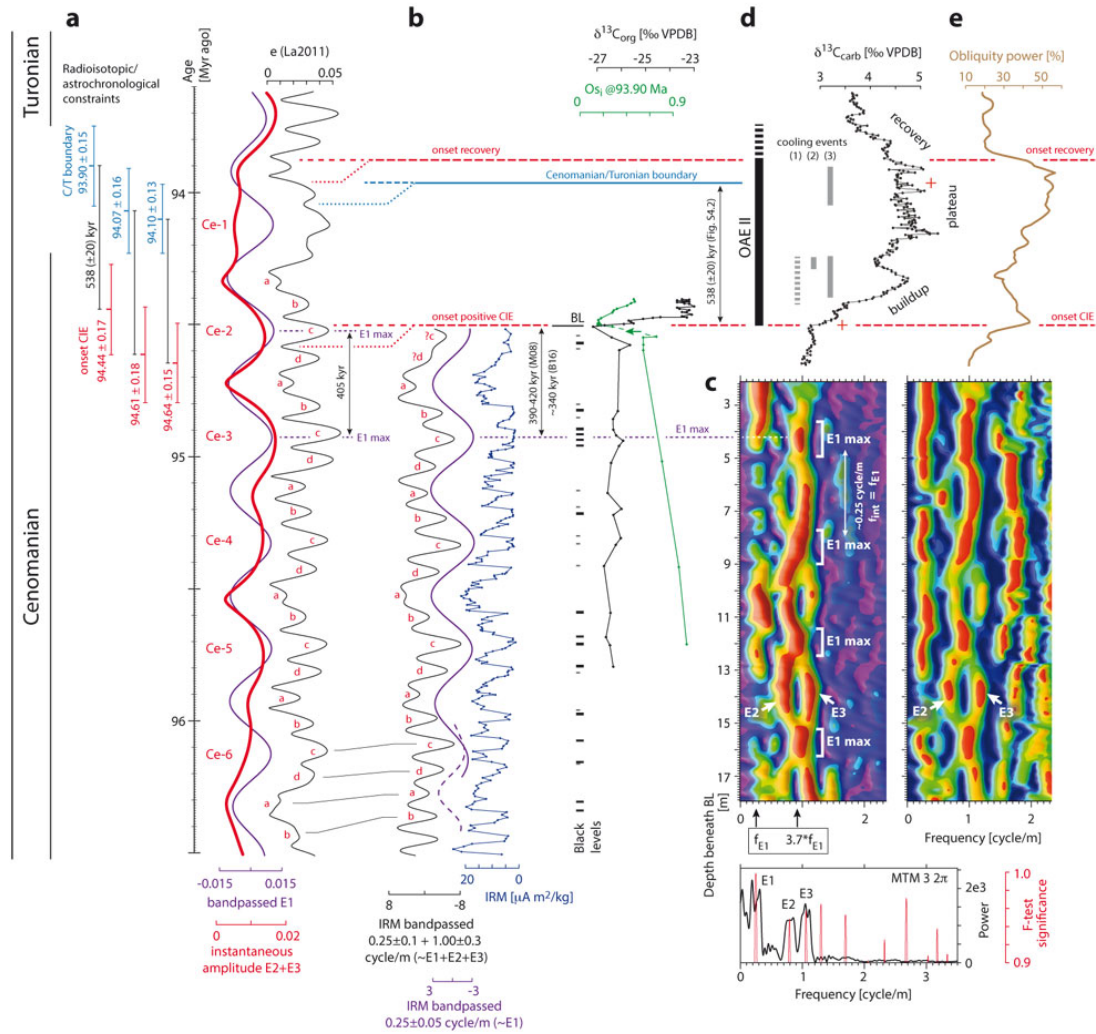


Figure 6. Eccentricity signature in the Cenomanian at Furlo. **(a)** Geochronology and the La2011 solution (Laskar et al. 2011b): bulk eccentricity (black line), bandpassed 405-kyr term (2.5 ± 0.5 cycle/Myr, Gaussian; purple line) and instantaneous amplitude of short eccentricity (Hilbert transformed 9.5 ± 3.0 cycle/Myr, Gaussian; thick red line). Maxima in E1 (405 kyr) eccentricity are labelled Ce-1 through Ce-6 and superimposed maxima in short eccentricity are labelled a through d. Ages of the Cenomanian-Turonian boundary (C/T; 93.90 ± 0.15 Ma; Meyers et al., 2012a; 94.10 ± 0.13 or 94.07 ± 0.16 Ma; Eldrett et al. 2015), bentonite A ($94.27 \pm 0.16/-0.17$ Ma; Meyers et al. 2012a) and the onset of positive carbon-isotope excursion (CIE; estimated by adding 538 ± 20 kyr to the age of the C/T boundary; Fig. S4.2) constrain the timing of OAE II. The uncertainty in numerical timing is too large to identify the phasing of OAE II relative to the E1 phases in La2011. The relative timing of the onset of CIE vs. C/T is, however, determined with a much smaller uncertainty, ± 20 kyr (Fig. S4.2). The major magmatic pulse documented in osmium isotopes (Turgeon and Creaser 2008) predates the onset of positive CIE by ~ 40 kyr (phase 'ii' in Du Vivier et al. 2014; green arrow in Fig. 6b). The numerical age of 405-kyr maxima and minima in La2011 is uncertain within ± 80 kyr (Fig. S4.3e); this uncertainty, however, does not affect the interpretation of 405-kyr phasing during OAE II. **(b)** Furlo section: IRM (blue line; Lanci et al. 2010), sum of bandpassed eccentricity

terms ($E1+E2+E3$; $0.25\pm0.10 + 1.00\pm0.3$ cycle/m, Gaussian; black line), bandpassed 405-kyr term (purple line: 0.25 ± 0.05 cycle/m Gaussian filter; dashed purple line: 0.30 ± 0.15 cycle/m Gaussian filter), $\delta^{13}C_{org}$ (black line; [Jenkyns et al. 2007](#)) and osmium-isotope data (green line; [Du Vivier et al. 2014](#)). Furlo section data are plotted against stratigraphic depth (scale as in [Fig. 6c](#)). Black shale and chert levels are plotted as horizontal lines to the right of the IRM data, after [Lanci et al. \(2010\)](#). BL = base of Bonarelli Level. The IRM curve is flipped horizontally and adjusted linearly to optimize the correlation of interpreted 405-kyr eccentricity maxima ([Fig. 6c](#)) with the eccentricity maxima in La2011 (see [Figure S4.3](#)). It should be stressed that the interpretation of eccentricity maxima/minima is not affected by the potential instability of the La2011 solution, because the 405-kyr period is constant within 0.16 % ([Laskar et al. 2011a](#)). The timing of the onset of BL relative to the latest 405-kyr maximum captured by FM patterns in EHA ([Fig. 6c](#)) is estimated using published age models: 390-420 kyr ([Mitchell et al. 2008](#); M08; dashed correlation line), and ~340 kyr (tuning #2 of Batenburg et al. 2016; B16; dotted correlation line). **(c)** EHA amplitude (left) and F-test significance (right) spectra of IRM (MTM $3\ 2\pi$; 4 m window, color scales as in [Fig. 7](#)). MTM power spectrum and F-test significance for the entire interval are shown at the bottom. Junctions in the $E2+E3$ trace occur systematically, in the same rhythm as the $E1$ signal and are therefore interpreted as 405-kyr maxima ($E1$ max). **(d)** $\delta^{13}C_{carb}$ signature of OAE II, Eastbourne section ([Paul et al. 1999](#)), calibrated in the time domain ([Figure S4.2](#); red crosses indicate age control points). The timing of cooling events in Europe and proto-Atlantic: 1 = TEX_{86} cooling in the North Atlantic ([Forster et al. 2007](#); [Sinninghe Damsté et al. 2010](#); [van Helmond et al. 2014](#)), 2 = plenus cool fauna in Europe ([Voigt et al. 2006](#)), 3 = $\delta^{18}O_{carb}$, Eastbourne ([Gambacorta et al. 2015](#)). **(e)** Changes in the power attributed to axial obliquity (Site 1261B, tropical Atlantic) calibrated in the time domain and anchored at the base of the positive CIE ([Meyers et al. 2012b](#)).

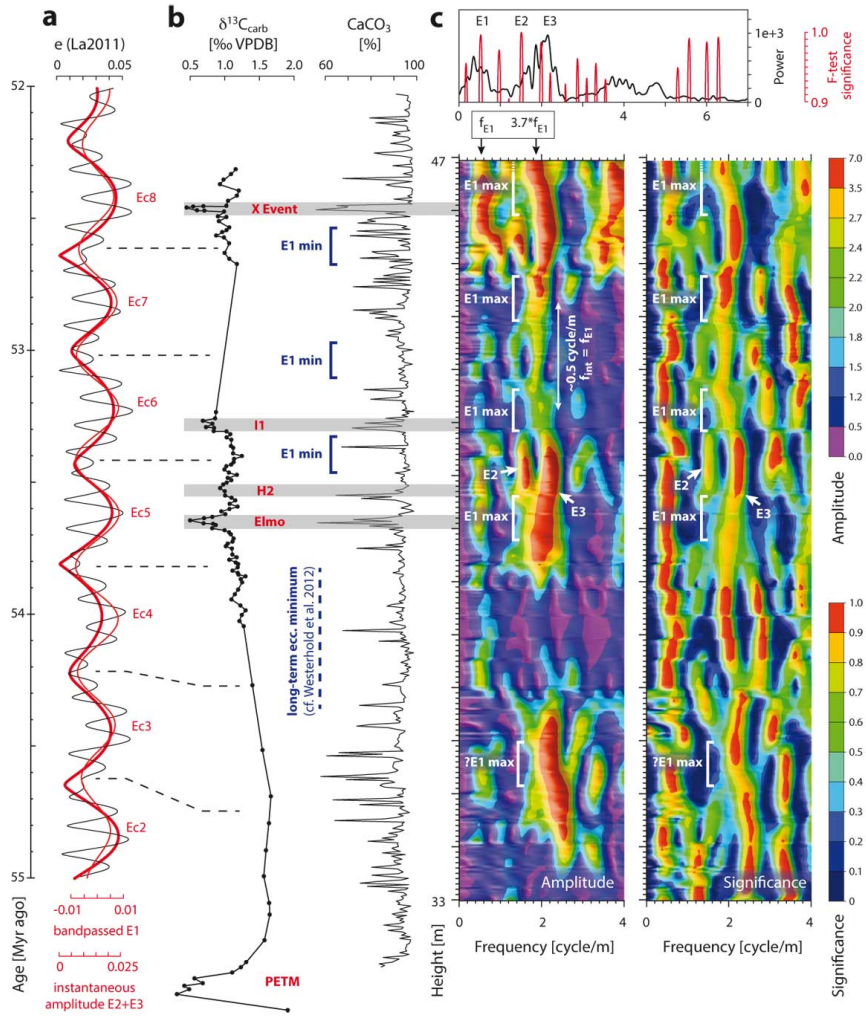


Figure 7. Eccentricity signature in the Lower Eocene, Contessa. **(a)** Total eccentricity (black), bandpassed 405-kyr term (2.5+0.5 cycle/Myr, Gaussian; thin red) and instantaneous amplitude of short eccentricity (Hilbert transformed 9.5±2.5 cycle/Myr, Gaussian; thick red) in the solution La2011 (Laskar et al. 2011b). Maxima in 405-kyr eccentricity are labelled Ec2 through Ec8 following Westerhold et al. (2012). **(b)** $\delta^{13}\text{C}_{\text{carb}}$ signatures of Eocene hyperthermals (gray bands), and high-resolution CaCO_3 data, Contessa Road section (Galeotti et al. 2010). **(c)** Time-series analysis of the CaCO_3 data: MTM power spectrum and F-test significance for the whole interval (MTM $3\ 2\pi$; top); EHA amplitude and probability spectra (MTM $3\ 2\pi$; 5 m window; bottom). The trace of the E2+E3 signal exhibits systematic alternations of intervals of positive and negative interference, in the upper part of the section. These junctions and bifurcations exhibit the same rhythm as the E1 signal and are therefore interpreted as maxima and minima, respectively, of the 405-kyr eccentricity cycle (cf. Figs. 1, 3, 4, and S1). The E2+E3 signal is poorly distinguishable in the interval 36.5–39 m, coincident with a minimum in the very long-term cycle of eccentricity modulation in La2011 (thick red line in Fig. 7a; cf. Westerhold et al. 2012). The interval is linearly adjusted so that E1 maxima in La2011 are aligned with the interpreted E1 maxima (E1 max). This tuning suggests that the major hyperthermals (except the PETM, which can not be evaluated here) occur at or near the maxima in 405-kyr eccentricity.